The Investigation on the Beam Spatial Intensity Distributions in the Injection-Seeded Terahertz Parametric Generator
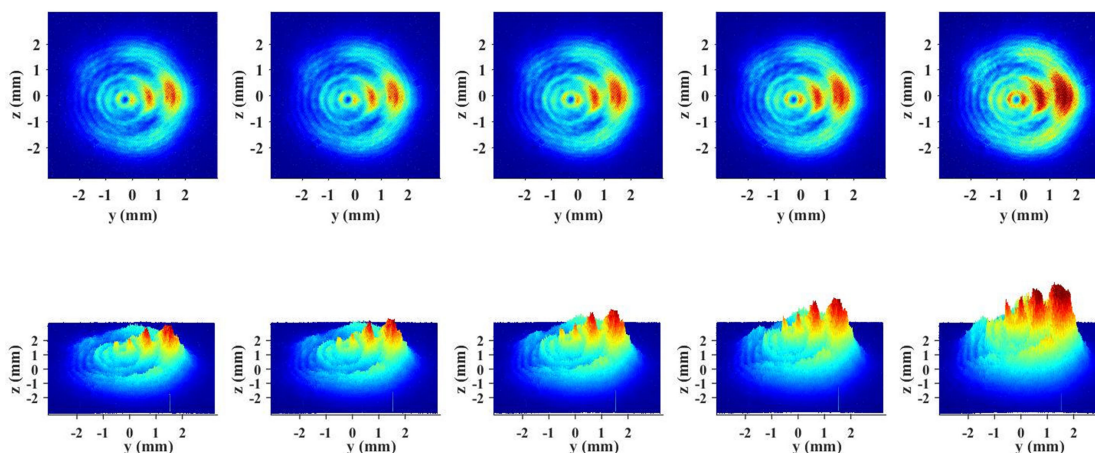
Jie Zang
Dong Wu
Xingyu Zhang
Zhenhua Cong
Zengguang Qin
Xiaohan Chen
Zhaojun Liu
Ping Li
Feilong Gao
Chenyang Jia
Yue Jiao
Weitao Wang
Shaojun Zhang

The Investigation on the Beam Spatial Intensity Distributions in the Injection-Seeded Terahertz Parametric Generator

Jie Zang [ID],[1] Dong Wu,[2] Xingyu Zhang,[1] Zhenhua Cong,[1]
Zengguang Qin,[1] Xiaohan Chen,[1] Zhaojun Liu,[1] Ping Li,[1]
Feilong Gao,[1] Chenyang Jia,[1] Yue Jiao,[1] Weitao Wang [ID],[3]
and Shaojun Zhang[4]

[1]School of Information Science and Engineering, Shandong Provincial Key Laboratory of
Laser Technology and Application, Shandong University, Jinan 250100, China
[2]Optoelectronics Research Centre, University of Southampton, Southampton SO17 1BJ,
U.K.
[3]Laser Institute of Shandong Academy of Sciences, Jinan 250014, China
[4]State Key Laboratory of Crystal Materials, Shandong University, Jinan 250100, China

Abstract: In terahertz (THz) wave parametric sources, the large angle between the pump and terahertz waves (about 65° in LiNbO$_3$ crystal) will affect the spatial intensity distributions. To investigate how the noncollinear phase-matching affects the spatial intensity properties of the pump, Stokes, and THz waves, we take the injection-seeded THz-wave parametric generator (is-TPG) as an example to study the beam spatial intensity properties via the numerical solutions of the coupled-wave equations. The simulated results demonstrate that the pump and Stokes intensities have significant changes along the THz-wave propagation direction. It is the first time that the spatial intensity distributions of the three waves in the THz-wave parametric sources have been studied in theory. In addition, the output intensity distributions of the pump, Stokes, and THz waves are measured in the designed is-TPG. The measured spatial intensity distributions are in coincidence with the simulated results. Investigations on the beam spatial intensity properties provide a potential approach to improve the THz-wave outputs and the pump conversion efficiency for the is-TPG and other THz-wave parametric sources.

Index Terms: Terahertz radiation, nonlinear optics, stimulated polariton scattering, LiNbO$_3$.

1. Introduction

Terahertz (THz) wave spectroscopy and spectral imaging have been widely applied to non-destructive identifications [1], [2] and biomedical diagnostics [3], [4]. THz-wave radiation sources play an important part in the development of these applications. During the past twenty years, THz-wave parametric sources have attracted much interest in generating coherent and frequency-
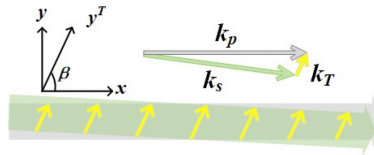
Fig. 1. The beam overlap between the pump beam (grey arrow), the Stokes beam (green arrow), and the THz beam (yellow arrow).

tunable THz radiations based on stimulated polariton scattering (SPS). There have been a variety of studies on different types of THz-wave parametric resources, such as the injection-seeded THz-wave parametric generator (is-TPG) [5], [6] and the THz-wave parametric oscillator (TPO) [7], [8]. Meanwhile, available nonlinear crystals for the THz-wave parametric source have been investigated, including $LiNbO_3$, $KTiOPO_4$, $KTiOAsO_4$, and $RbTiOPO_4$ [9]–[12]. Besides, a simple analytical formula for the THz-wave parametric gain in theory has been derived by solving the coupled-wave equations [13], [14].

In the THz-wave parametric source, when a near-infrared pump photon is consumed, a photon at THz frequency and a near-infrared Stokes photon are generated. Because of the huge difference between the pump/Stokes refractive index ($n_{p/s} \sim 2.2$) and the THz-wave refractive index ($n_T \sim 5.2$), only non-collinear phase-matching condition could be fulfilled. The angle between the pump and terahertz waves is rather large, for example, the angle is about $65°$ in $LiNbO_3$ crystal [15]. Due to limited beam sizes, the interaction between the three beams is confined to the overlapped area. When the crystal length is obviously longer than the beam size, the spatial separations between the THz-wave and pump beams will happen, and the interaction between them will certainly diminish simultaneously. So the contributing interaction length for the THz-wave is determined by the limited overlapping size and the large angle between them, instead of the whole crystal length. Meanwhile, the pump and Stokes intensities will change along the THz-wave propagation direction. They will influence the spatial intensity distribution of the generated THz-wave subsequently, because the THz-wave parametric gain mainly depends on the pump and Stokes intensities. In another word, the angle between the pump and terahertz waves changes the beam spatial intensity distributions in the THz-wave parametric source.

So far, the spatial intensity distributions caused by the non-collinear phase-matching have not been investigated in detail, but they are in need of studies. Because they can provide guidance on how to optimize the THz-wave parametric source to enhance the THz-wave output energy. In this paper, we take is-TPG as an example to obtain the beam spatial intensity properties of the pump, Stokes, and terahertz waves from the numerical solutions of the coupled-wave equations. The simulation method and results are explained clearly in Section 2. In addition, we have measured the output energy densities of the three waves in the designed experimental system of is-TPG. The comparison of the experimental and simulated results is given in Section 3.

2. Theory

2.1 Coupled-Wave Equations

The non-collinear phase-matching condition ($\mathbf{k}_p = \mathbf{k}_s + \mathbf{k}_T$) in the is-TPG is schematically shown in Fig. 1. The pump beam propagates along the x-axis of the crystal and the generated THz-wave propagates in the y^T direction, with an angle β to the x-axis inside the crystal. When the THz-wave frequency is 1.58 THz, the angle β is $65°$ in the $LiNbO_3$ crystal. The angle between the Stokes and pump beams is so small that the Stokes propagation direction can be treated as parallel to the x-axis.

The three waves are all polarized along the z-axis. The electric fields are represented as the products of the complex amplitudes and the plane-waves at their centre frequencies:

$$E_p = E(\omega_p) + c.c. = A_p(x) \exp[i(k_p x - \omega_p t + \varphi_p)] + c.c., \tag{1a}$$

$$E_s = E(\omega_s) + c.c. = A_s(x) \exp\left[i(k_s x - \omega_s t + \varphi_s)\right] + c.c., \tag{1b}$$

$$E_T = E(\omega_T) + c.c. = A_T(y^T) \exp\left[i(k_T y^T - \omega_T t + \varphi_T)\right] + c.c., \tag{1c}$$

where A_p, A_s, and A_T are the complex amplitudes of the pump, Stokes, and terahertz waves.

The coupled-wave equations start from:

$$\left[\nabla^2 + \frac{\omega^2}{c^2}\varepsilon^{(1)}(\omega)\right] E(\omega) = \frac{\omega^2}{c^2 \varepsilon_0} P^{NL}(\omega), \tag{2}$$

where $\varepsilon^{(1)}$ is the dielectric constant and P^{NL} is the nonlinear polarization term. $\varepsilon^{(1)}$ is frequency-dependent and can be represented as [16]:

$$\varepsilon^{(1)}(\omega) = \varepsilon_\infty + \sum_m S_m \frac{\omega_{mTO}^2}{\omega_{mTO}^2 - \omega^2 - i\Gamma_{mTO}\omega}, \tag{3}$$

where ε_∞ is the high-frequency dielectric constant. ω_{mTO}, S_m, and Γ_{mTO} are the frequency, strength, and linewidth of the mth TO mode in the nonlinear crystal. The dielectric constant $\varepsilon^{(1)}$ is related to the absorption coefficient and the reflective index. The macroscopic nonlinear polarization P^{NL} can be obtained from Garrett's anharmonic vibration oscillator theory shown as [17]:

$$P_p^{NL} = \varepsilon_0 \left(\chi^{(2)} E_s E_T + \chi^{(3)} |E_s|^2 E_p\right), \tag{4a}$$

$$P_s^{NL} = \varepsilon_0 \left(\chi^{(2)} E_p E_T^* + \chi^{(3)} |E_p|^2 E_s\right), \tag{4b}$$

$$P_T^{NL} = \varepsilon_0 \chi^{(2)} E_p E_s^*, \tag{4c}$$

where $\chi^{(2)}$ and $\chi^{(3)}$ are the second and third order nonlinear susceptibilities. $\chi^{(2)}$ can be represented as [18], [19]:

$$\chi^{(2)} = \chi_e^{(2)} + \chi_i^{(2)} = 4d_{33} + \chi_i^{(2)}, \tag{5}$$

where $\chi_e^{(2)}$ and $\chi_i^{(2)}$ are the second order electronic and ionic susceptibilities. $\chi_e^{(2)}$ is related to the second-harmonic nonlinear coefficient d_{33}. $\chi_i^{(2)}$ is the combined ionic responses of all the infrared- and Raman-active TO modes which are contributing in the SPS. The numerical value of $\chi_i^{(2)}$ is an order of magnitude larger than the $\chi_e^{(2)}$ [20].

Substituting Eqs. (3)–(5) into Eq. (2), the coupled-wave equations represented in the electric fields can be obtained [13], [14]. For the parametric process, the initial phase difference $\triangle\varphi = \varphi_p - \varphi_s - \varphi_T$ is defined as $-\pi/2$ [21]. Based on the relations between the intensity and the electric field amplitude $I = 2c\varepsilon_0 n|A|^2$, the coupled-wave equations represented in the intensities can be written as:

$$\frac{dI_p}{dx} = \frac{2\pi}{n_p \lambda_p}\left[-\frac{\kappa^{(2)}}{\sqrt{2c\varepsilon_0 n_s n_T / n_p}}\left(I_p I_s I_T\right)^{1/2} - \kappa^{(3)} I_p I_s\right], \tag{6a}$$

$$\frac{dI_s}{dx} = \frac{2\pi}{n_s \lambda_s}\left[\frac{\kappa^{(2)}}{\sqrt{2c\varepsilon_0 n_p n_T / n_s}}\left(I_p I_s I_T\right)^{1/2} + \kappa^{(3)} I_p I_s\right], \tag{6b}$$

$$\frac{dI_T}{dy^T} = \frac{2\pi}{n_T \lambda_T}\left[-\alpha_T I_T + \frac{\kappa^{(2)}}{\sqrt{2c\varepsilon_0 n_p n_s / n_T}}\left(I_p I_s I_T\right)^{1/2}\right], \tag{6c}$$

where

$$\alpha_T = \text{Im}[\varepsilon^{(1)}(\omega_T)], \tag{7a}$$

$$\kappa^{(2)} = 4d_{33} + \text{Re}[\chi_i^{(2)}], \tag{7b}$$

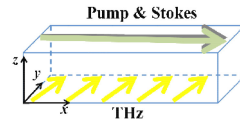$$\kappa^{(3)} = \text{Im}[\chi_i^{(2)}]. \tag{7c}$$

Fig. 2. The whole interaction block. The length along the x-axis is same with the crystal length. The yz-plane is the overlap between the pump and Stokes beams. The output plane of the pump/Stokes wave is the yz-plane, while the THz-wave output plane is the xz-plane.
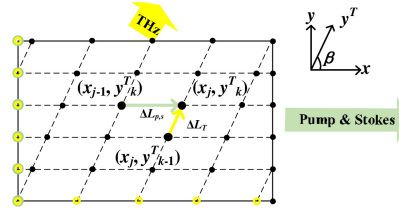

Fig. 3. The interaction area on the *xy*-plane. Every position (displayed in black dot) has a coordinate (x, y^T). The distances are decided by the propagation lengths of $\Delta L_{p,s}$ ($\Delta L_{p,s} = c\Delta t/n_{p,s}$) and ΔL_T ($\Delta L_T = c\Delta t/n_T$). The pump and Stokes beams are degenerated here, and they are regarded to travel along the same trace (green arrow) along the *x*-axis. The THz-wave (yellow arrow) propagates in the y^T direction. The green and yellow circles represent the input boundary positions of the pump/Stokes and terahertz waves.

α_T is related to the THz-wave absorption coefficient in the crystal. $\kappa^{(2)}$ and $\kappa^{(3)}$ correspond to the second and third order nonlinear coefficients. All the coefficients are frequency-depended. For a given THz-wave frequency, the coupled-wave equations could be solved by a general method for the nonlinear ordinary differential equations (ODEs) [22], [23].

2.2 Simulation Method

The is-TPG is consisted of a pulse pump laser with the pulse width of t_p, a CW Stokes seed laser, and a LiNbO$_3$ crystal. The overlap region between the three beams is described as a cuboid interaction block as shown in Fig. 2. The pump and Stokes beams are displayed in the green arrow, propagating along the same trace, while the THz-wave propagates along the yellow arrow. The output plane of the pump/Stokes beam is the *yz*-plane, while the THz-wave output plane is the *xz*-plane. The interaction block length along the *x*-axis is corresponding to the crystal length. The area of the *yz*-plane is the overlap between the pump and Stokes beams.

Because the z-axis intensity distributions are not influenced by the non-collinear phase-matching condition, so the interaction area is displayed in the *xy*-plane in Fig. 3. Every position (displayed in black dot) has a coordinate (x, y^T). Over a time interval $\Delta t\,(\Delta t \ll t_p)$, the pump/Stokes wave propagates from position (x_{j-1}, y_k^T) to (x_j, y_k^T) shown as the green arrow, while the THz-wave propagates from position (x_j, y_{k-1}^T) to (x_j, y_k^T) displayed as the yellow arrow. The distances between the positions are decided by the propagation lengths over the time interval Δt. The propagation lengths for the pump/Stokes and terahertz waves are more specifically defined as $\Delta L_{p,s} = c\Delta t/n_{p,s}$ and $\Delta L_T = c\Delta t/n_T$ respectively. In the numerical calculation, the time step Δt is minimized to make sure the interaction lengths are small enough for the coupled-wave equations to converge. The green and yellow circles represent the input boundary positions of the pump/Stokes and terahertz waves respectively.

The intensities of the input boundary positions are given by:

$$I_p(0, y_k^T) = I_{pump}(t), \tag{8a}$$

$$I_s(0, y_k^T) = I_{seed}(t), \tag{8b}$$

$$I_T(0, y_k^T) = I_T(x_j, 0) = 0, \tag{8c}$$

TABLE 1
The Parameters in the Coupled-Wave Equations

	Parameter	Value
α_T	Dispersion absorption coefficient	0.820
$\kappa^{(2)}$	Second order nonlinear coefficient	8.257×10^{-10} m/V
$n_{p,s}$	Refractive index of pump and Stokes waves	2.139
n_T	Refractive index of THz-wave	5.020
λ_p	Wavelength of pump wave	1.064×10^{-6} m
λ_s	Wavelength of Stokes wave	1.070×10^{-6} m
λ_T	Wavelength of THz-wave	1.897×10^{-4} m
β	Angle between the pump and terahertz waves	1.121 rad

where $I_{pump}(t)$ and $I_{seed}(t)$ are the time-dependent intensities of the input pump laser and Stokes seed laser. Except for the input boundary positions, the intensity of any position is decided by the intensity of the last position and the intensity increment over the interaction length. Neglecting $\kappa^{(3)}$ ($\kappa^{(3)} \ll \kappa^{(2)}$ at 1.58 THz) in Eqs. (6) and (7), the intensities of the pump, Stokes, and terahertz waves at any position (x_j, y_k^T) are given by:

$$I_p(x_j, y_k^T) = I_p(x_{j-1}, y_k^T) - \Delta I_p(\Delta L_p), \tag{9a}$$

$$I_s(x_j, y_k^T) = I_s(x_{j-1}, y_k^T) + \Delta I_s(\Delta L_s), \tag{9b}$$

$$I_T(x_j, y_k^T) = I_T(x_j, y_{k-1}^T) + \Delta I_T(\Delta L_T), \tag{9c}$$

where

$$\Delta I_p(\Delta L_p) = \frac{2\pi\kappa^{(2)}}{n_p \lambda_p \sqrt{2c\varepsilon_0 n_s n_T / n_p}} \left[I_p(x_{j-1}, y_k^T) I_s(x_{j-1}, y_k^T) I_T(x_j, y_{k-1}^T) \right]^{1/2} \Delta L_p, \tag{10a}$$

$$\Delta I_s(\Delta L_s) = \frac{2\pi\kappa^{(2)}}{n_s \lambda_s \sqrt{2c\varepsilon_0 n_p n_T / n_s}} \left[I_p(x_{j-1}, y_k^T) I_s(x_{j-1}, y_k^T) I_T(x_j, y_{k-1}^T) \right]^{1/2} \Delta L_s, \tag{10b}$$

$$\Delta I_T(\Delta L_T) = \frac{2\pi}{n_T \lambda_T} \left\{ -\alpha_T I_T(x_j, y_{k-1}^T) + \frac{\kappa^{(2)}}{\sqrt{2c\varepsilon_0 n_p n_s / n_T}} \left[I_p(x_{j-1}, y_k^T) I_s(x_{j-1}, y_k^T) I_T(x_j, y_{k-1}^T) \right]^{1/2} \right\} \Delta L_T. \tag{10c}$$

By solving Eqs. (9) and (10) for all the positions, we can obtain the intensity distributions in the whole interaction area. In fact, the intensity is the power density in the unit of W/cm^2.

2.3 Simulation Results

The pump and Stokes beam spots are assumed in the shape of square with the side length of 4.5 mm. The crystal length along the x-axis is set as 5.5 cm. Consequently, the whole interaction block used in the subsequent calculation has the size of 5.5 cm (x) × 4.5 mm (y) × 4.5 mm (z). The parameter values in the coupled-wave equations are given in Table 1. d_{33} has a value of 25.0 pm/V at 1.064 μm in 5.0 mol % MgO:LiNbO$_3$ [24].

2.3.1 Rectangular Pump Pulse Profile: A rectangular pulse is used as the incident pump profile in Fig. 4, and the pulse width is $t_p = 7.0$ ns. The pump and Stokes beams propagate from x = 0 cm to x = 5.5 cm. The THz-wave propagates from y = 0 mm to y = 4.5 mm and $\beta = 65°$. When the front edge of the pump pulse gets to x = 5.5 cm, the intensity distributions on the xy-plane are shown as Fig. 4. The pump energies are 115 mJ, 120 mJ, and 125 mJ respectively. The input seed power is 200 mW. To demonstrate the intensity distributions clearly, the three waves are illustrated from
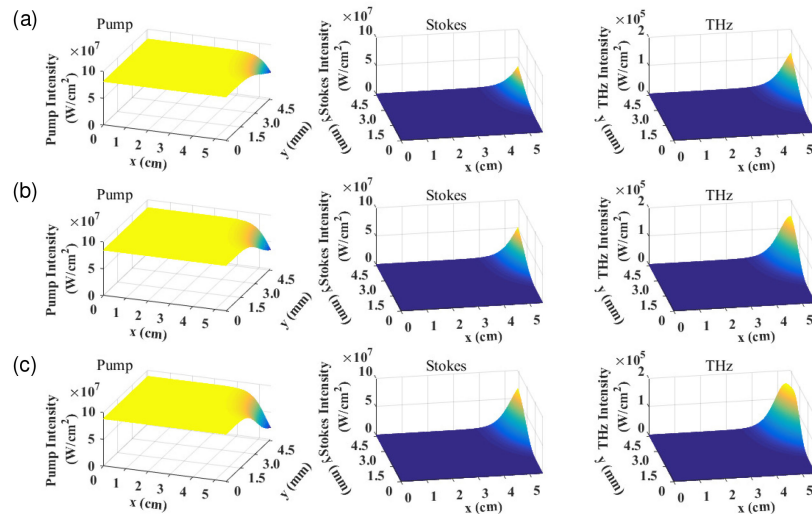
Fig. 4. The intensity distributions of the pump, Stokes, and terahertz waves on the *xy*-plane at the pump energies of (a) 115 mJ, (b) 120 mJ and (c) 125 mJ. The input seed power is 200 mW. To demonstrate the intensity distributions clearly, the three waves are illustrated from different viewpoints. The pump and Stokes beams propagate from $x = 0$ cm to $x = 5.5$ cm. The THz-wave propagates from y = 0 mm to y = 4.5 mm and the angle between the THz-wave and pump beam is 65°.

different viewpoints. As we can see, the Stokes and terahertz waves have sustained growth with increasing *x* and *y*, while the pump is consumed along the *x*-and *y*-axes. When *x* and *y* are large, the Stokes and THz-wave intensities increase rapidly, and the pump intensity is consumed sharply. When the input pump energy increases, the pump depletion is more obvious, and the Stokes and THz-wave intensities have more obvious growths. Although the incident pump and Stokes seed intensities are uniformly distributed along the *y*-axis at $x = 0$ cm, the output intensities distributions of all the three waves (at $x = 5.5$ cm) are not uniform anymore.

2.3.2 Gaussian Pump Pulse Profile: A Gaussian pulse is used as the incident pump profile, and the full width at half maximum (FWHM) of the Gaussian pulse is $t_p = 7.0$ ns. The pump and Stokes beams propagate from $x = 0$ cm to $x = 5.5$ cm. The THz-wave propagates from $y = 0$ mm to $y = 4.5$ mm and $\beta = 65°$. In Figs. 5(a) and (b), the seed power is 200 mW and the pump energy is 130 mJ. Fig. 5(a) depicts the *x*-axis power density distributions of the pump, Stokes, and terahertz waves in the whole interaction time at $y = 4.5$ mm. As we can see, the pump intensities are depleted along the *x*-axis at the peak time of the pump pulse, while the Stokes intensities have sustained growth along the *x*-axis. Meanwhile, the THz-wave intensities have obvious growth with increasing *x*. Fig. 5(b) depicts the *y*-axis power density distributions of the three waves in the whole interaction time at $x = 5.5$ cm. With increasing *y*, the pump intensity is rapidly depleted, and the Stokes and THz intensities increase obviously. In Figs. 5(c) and (d), the seed power is 200 mW and the pump energy is 140 mJ. In Fig. 5(c) the *x*-axis intensity distributions are shown in the whole interaction time when $y = 4.5$ mm. In Fig. 5(d) the *y*-axis intensity distributions are demonstrated in the whole interaction time when $x = 5.5$ cm. We can see that, near $x = 5.5$ cm and $y = 4.5$ mm, the THz-wave intensity appears to decrease while the pump intensity decreases obviously and the Stokes intensity has saturation phenomenon.

In fact, the intensity is the power density. By integrating the output power densities over the whole interaction time, the output energy density could be obtained. Fig. 6 depicts the normalized output energy density distributions of the pump, Stokes, and terahertz waves. The output energy density distributions of the pump and Stokes waves are represented by the *y*-axis energy density distributions at $x = 5.5$ cm. The THz-wave output energy density distribution is represented by the *x*-axis energy density distribution at $y = 4.5$ mm. The input seed power is 200 mW. The pump
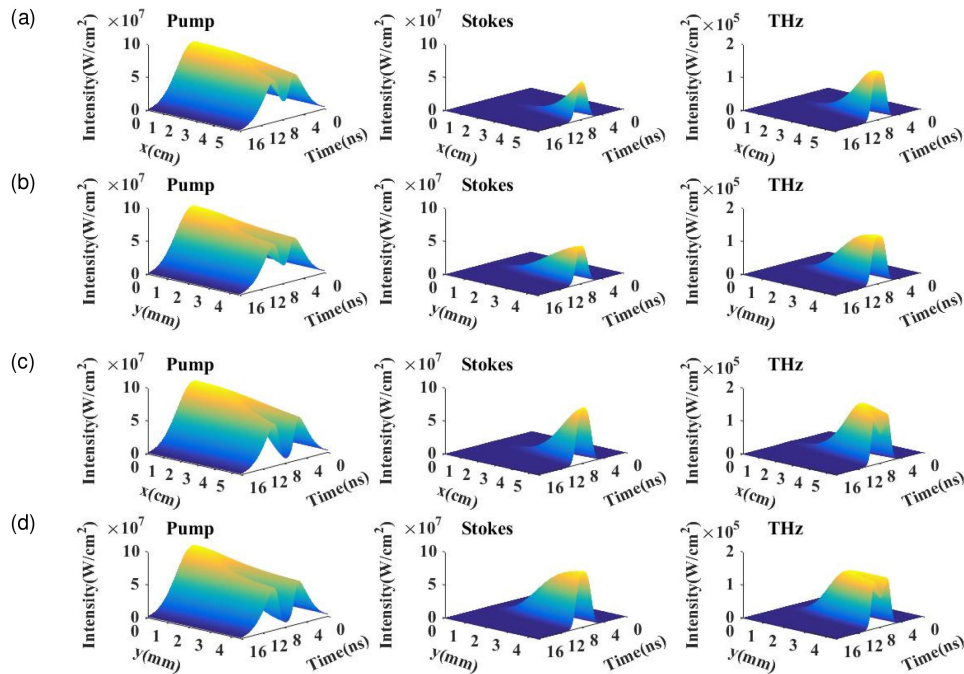
Fig. 5. The *x*-axis and *y*-axis intensity distributions of the pump, Stokes, and terahertz waves in the whole interaction time. The pump energies are (a) 130 mJ, (b) 130 mJ, (c) 140 mJ, and (d) 140 mJ. The input seed power is 200 mW.
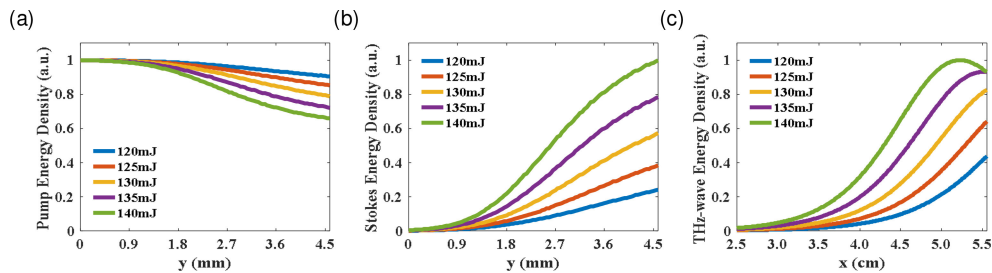

Fig. 6. The output energy density distributions of the (a) pump, (b) Stokes, and (c) terahertz waves.

energies are 120, 125, 130, 135 and 140 mJ respectively. In Fig 6(a), the pump energy density decreases along the *y*-axis, and the pump depletion is more obvious with increasing input pump energy. In Fig 6(b), the Stokes energy density increases with increasing *y*, and the saturation phenomena appear when *y* is large, because of the pump depletion along the *y*-axis. In Fig 6(c), the THz-wave energy density gets larger with increasing *x*, but it declines at $x = 5.5$ cm when the pump energy is 140 mJ, due to the obvious pump depletion along the *x*-axis.

3. Experimental Results and Discussions

Two LiNbO$_3$ crystals were employed separately in the experiment. Both LiNbO$_3$ crystals were doped with 5.0 mol % MgO. One was in the shape of cuboid and had the size of 50 mm (*x*) × 5 mm (*y*) × 5 mm (*z*). The cuboid LiNbO$_3$ cyatal was used to measure the intensities of the output pump and Stokes beams as shown in Fig. 7(a). The other LiNbO$_3$ crystal was in the shape of isosceles trapezoid as shown in Fig. 7(b). The long base and legs were in the lengths of 65 mm and 37 mm. The base angles were 65°. The *z*-axis thickness was 7 mm. At the long base, the THz-
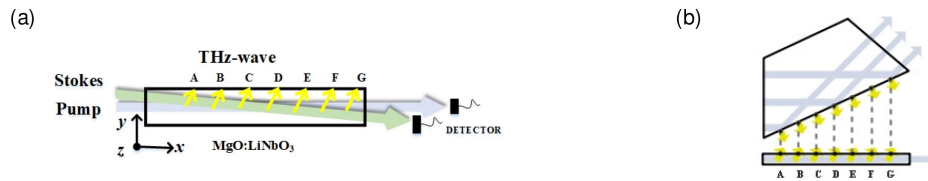
Fig. 7. The cubiod and isosceles trapezoid LiNbO$_3$ crystals used in the experiment. (a) The cubiod cryastal was used to measure the intensities of the output pump and Stokes beams. (b) The isosceles trapezoid crystal was used to measure the THz intensity distribution along the x-axis by the measurement of the THz intensity along the emitting edge. The yellow, green, and grey arrows represent the THz, Stokes, and pump beams. The dots connected by the same dash line have the same length along the x-axis.
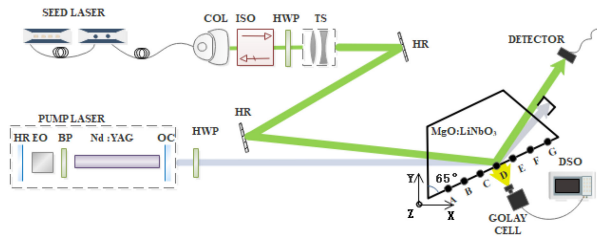

Fig. 8. The experimental setup of the surface-emitted is-TPG. HR is the highly reflective mirror at 1060–1090 nm; EO is the electro-optic Q-switch cell; BP is the beam polarizer; OC is the Gaussian output mirror; HWP is the half-wave plate; COL is the collimator; ISO is the isolator; TS is the Galilean-telescope.

wave is emitted perpendicularly to the surface, while the pump and Stokes beams are reflected. The surface-emitted configuration enables the measurement of the THz-wave intensigy along the emitting edge of the crystal. By changing the pump beam input position, the interaction length along the x-axis could be changed, so the THz-wave intensity distribution along the x-axis could be obtained. The THz-wave intensity distribution measured along the emitted edge is equivalent to the THz intensity distribution on the THz-wave output plane of the cuboid LiNbO$_3$ in Fig. 7(a). The detailed corresponding relationship is also shown schematically in Fig. 7(b). The points A, B, C, D, E, F, and G correspond to different x values as 2.5, 3.0, 3.5, 4.0, 4.5, 5.0, and 5.5 cm respectively. The yellow and grey arrows represent the THz and pump beams. The dots connected by the same dash line have the same length along the x-axis.

The experimental setup of the surface-emitted is-TPG is represented in Fig. 8. The pump laser was a Q-switched Nd:YAG laser at 1064 nm. The pulse width, repetition frequency and beam diameter were 7.0 ns, 1 Hz and 4.6 mm. The intensity distribution of the pump beam was similar to the Top-Hat distribution but it had intensity rings on the beam spot. A fiber laser source (NP Photonics, RFLS-25-1-1070) connected to an optical fiber amplifier (Amonics, AYDFA-UL-PM-30-B-FA) was utilized as the injected Stokes seed laser. The wavelength and line-width of the Stokes seed were 1070 nm and 3 kHz. A fixed-focus-collimator (THORLABS, F220APC) was used to produce the collimated beam, while a Galilean-telescope configuration was used to expand the seed beam into FWHM diameter of 4.9 mm. The input and output faces of all the crystals were anti-reflection (AR) coated at 1060–1090 nm ($T > 99.8\%$). The input pump beam propagated along the crystal x-axis while the internal angle between the Stokes and pump beams was 0.75°. The pump and Stokes energies were measured by an energy sensor (J-50MB-YAG, Coherent Inc.) connected to an energy meter (EPM2000, Coherent Inc.). The THz-wave energy was detected by a Golay Cell (GC-1D, TYDEX) connected to a digital oscilloscope (Tektronix DPO 4104B, 1 GHz, 8 GS/s). To block the scattered pump and Stokes waves, a THz low pass filter (LFP 14.3–47, TYDEX) was used in the experiment, of which the transmittance was about 80% at 1.58 THz. The output pump and Stokes beam profiles were captured by a CCD camera beam profiler (THORLABS, BC106N-VIS).
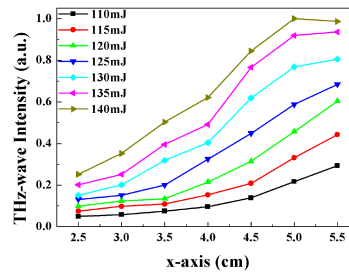
Fig. 9. The measured THz-wave output energy density distributions along the *x*-axis.
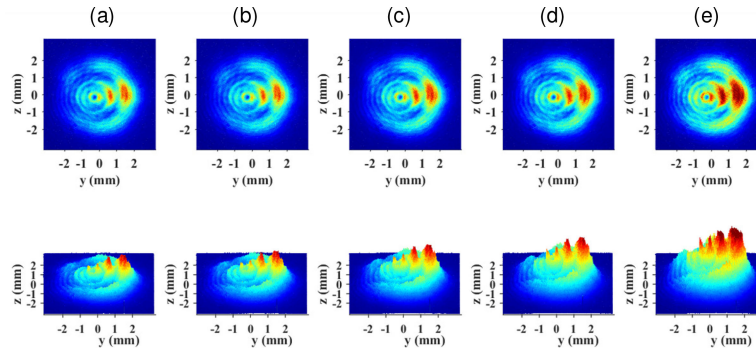

Fig. 10. The measured Stokes output energy density distributions at the pump energies of (a) 120 mJ, (b) 125 mJ, (c) 130 mJ, (d) 135 mJ, and (e) 140 mJ. The intensity rings are caused by the intensity rings of the input pump beams.
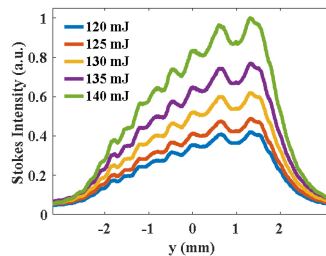

Fig. 11. The measured Stokes output energy density distributions along the *y*-axis. The intensity fluctuations are caused by the intensity rings of the input pump beams.

Fig. 9 shows the output THz-wave energy densities measured at points A, B, C, D, E, F, and G. Fig. 9 corresponds to the THz-wave output energy density distribution along the *x*-axis. The measured results are generally in agreement with the calculated results shown in Fig. 6(c). Both the experimental and simulated results demonstrate that the THz-wave intensities get larger with increasing *x*. And the THz-wave energy density decreases at $x = 5.5$ cm when the pump energy is 140 mJ and the Stokes seed power is 200 mW.

The energy density distributions of the output Stokes beams are depicted in Fig. 10. The seed power is 200 mW. The horizontal and vertical axes correspond to the *y*- and *z*-axes. $y = 0$ is set at the centre of the beam. The region from $y = -2.25$ mm to $y = 2.25$ mm corresponds to the region from $y = 0$ to $y = 4.5$ mm in Figs. 4–6. The energy density distributions along the *y*-axis are shown in Fig. 11. It is obvious that the measured Stokes energy densities increase with increasing *y*, and they have the same tendencies with the simulated results shown in Fig. 6(b). The intensity rings in
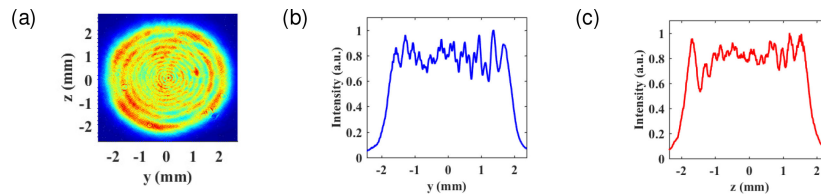
Fig. 12. (a) The energy density distributions of the input pump beam. (b) The *y*-axis and (c) *z*-axis energy density distributions of the pump beam.
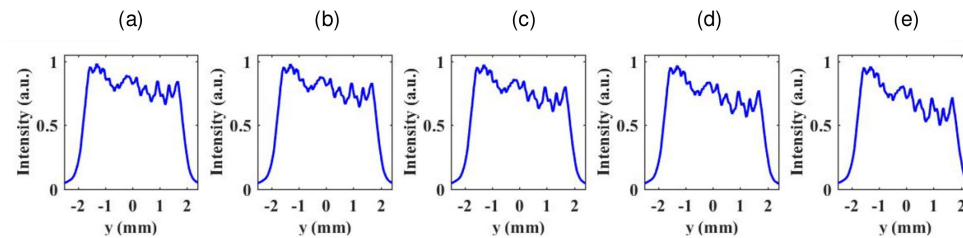

Fig. 13. The normalized *y*-axis energy density distributions of the output pump spots at the pump energies of (a) 120 mJ, (b) 125 mJ, (c) 130 mJ, (d) 135 mJ, and (e) 140 mJ.

Fig. 10 and the intensity fluctuations in Fig. 11 are caused by the intensity rings of the input pump beams.

The spatial energy density distribution of the input pump beam is shown in Fig. 12(a). The horizontal and vertical axes correspond to the *y*- and *z*-axes. Figs. 12(b) and (c) show the energy density distributions along the *y*- and *z*-axes respectively. The intensity distribution of the input pump beam is similar to the Top-Hat distribution, but it has intensity rings on the beam spot. The output pump energy density distributions are measured at the pump energies of 120 mJ, 125 mJ, 130 mJ, 135 mJ, and 140 mJ in the cuboid $LiNbO_3$ crystal. The seed power is 200 mW. They are represented by the normalized *y*-axis intensity distributions in Fig. 13. The output pump intensities decrease with increasing *y*, and they have the same tendencies with the simulated results shown in Fig. 6(a).

Both the experimental and simulated results demonstrate that the non-collinear phase- matching changes the pump and Stokes beam intensity distributions along the *y*-axis. The spatial intensity distribution changes will certainly influence the conversion efficiency. Studying the beam spatial intensity properties caused by the non-collinear phase-matching are beneficial to the optimizations of the is-TPG, TPO, and other THz-wave parametric sources. Based on these investigations on the spatial intensity distributions, the intensity profile and the diameter of the pump beam, the THz-wave coupling method, and the design of the nonlinear crystal are able to get optimized.

4. Conclusions

We obtain the simulated spatial intensities of the pump, Stokes, and terahertz waves in the is-TPG via the numerical solutions of the coupled-wave equations. The simulated results include the power density distributions in the whole interaction area and the output energy density distributions on the output planes. It is demonstrated that the non-collinear phase-matching has significant effects on the beam spatial intensity distributions. Meanwhile the output energy density distributions of the pump, Stokes, and terahertz waves are measured in the designed is-TPG. The experimental results have the same tendencies with the simulated results. Investigations on the beam spatial intensity properties provide a potential approach to improve the THz-wave output and the pump conversion efficiency for the is-TPG, TPO, and other THz-wave parametric sources.

References

[1] K. Kawase, Y. Ogawa, Y. Watanabe, and H. Inoue, "Non-destructive terahertz imaging of illicit drugs using spectral fingerprints," *Opt. Exp.*, vol. 11, no. 20, pp. 2549–2554, 2003.

[2] J. F. Federici *et al.*, "THz imaging and sensing for security applications-explosives, weapons and drugs," *Semicond. Sci. Technol.*, vol. 20, no. 7, pp. S266–S280, 2005.

[3] A. J. Fitzgerald, E. Berry, N. N. Zinovev, G. C. Walker, M. A. Smith, and J. M. Chamberlain, "An introduction to medical imaging with coherent terahertz frequency radiation," *Phys. Med. Biol.*, vol. 47, no. 7, pp. R67–R84, 2002.

[4] S. J. Oh *et al.*, "Molecular imaging with terahertz waves," *Opt. Exp.*, vol. 19, no. 5, pp. 4009–4016, 2011.

[5] G. Tang *et al.*, "Energy scaling of terahertz-wave parametric sources," *Opt. Exp.*, vol. 23, no. 4, pp. 4144–4152, 2015.

[6] K. Kawase, J. Shikata, K. Imai, and H. Ito, "Transform-limited, narrow-linewidth, terahertz-wave parametric generator," *Appl. Phys. Let.*, vol. 78, no. 19, pp. 2819–2821, 2001.

[7] A. J. Lee and H. M. Pask, "Continuous wave, frequency-tunable terahertz laser radiation generated via stimulated polariton scattering," *Opt. Lett.*, vol. 39, no. 3, pp. 442–445, 2014.

[8] R. Zhang, Y. Qu, W. Zhao, C. Liu, and Z. Chen, "Si-prism-array coupled terahertz-wave parametric oscillator with pump light totally reflected at the terahertz-wave exit surface," *Opt. Lett.*, vol. 41, no. 17, pp. 4016–4019, 2016.

[9] Y. Nakagomi, K. Suizu, T. Shibuya, and K. Kawase, "Multimode laser-pumped injection-seeded terahertz-wave parametric generator," *Jpn. J. Appl. Phys.*, vol. 49, no. 10, pp. 102701–102703, 2010.

[10] W. Wang *et al.*, "Terahertz parametric oscillator based on $KTiOPO_4$ crystal," *Opt. Lett.*, vol. 39, no. 13, pp. 3706–3709, 2014.

[11] W. Wang *et al.*, "THz-wave generation via stimulated polariton scattering in $KTiOAsO_4$ crystal," *Opt. Exp.*, vol. 22, no. 14, pp. 17092–17098, 2014.

[12] T. A. Ortega, H. M. Pask, D. J. Spence, and A. J. Lee, "Stimulated polariton scattering in an intracavity $RbTiOPO_4$ crystal generating frequency-tunable THz output," *Opt. Exp.*, vol. 24, no. 10, pp. 10254–10264, 2016.

[13] C. Henry and C. Garrett, "A theory of parametric gain near a lattice resonance," *Phys. Rev.*, vol. 171, no. 3, pp. 1058–1064, 1968.

[14] U. T. Schwarz and M. Maier, "Damping mechanisms of phonon polaritons, exploited by stimulated Raman gain measurements," *Phys. Rev. B*, vol. 58, no. 2, pp. 766–775, 1998.

[15] K. Kawase, J. Shikata, H. Minamide, K. Imai, and H. Ito, "Arrayed silicon prism coupler for a terahertz-wave parametric oscillator," *Appl. Opt.*, vol. 40, no. 9, pp. 1423–1426, 2001.

[16] A. S. Barker and R. Loudon, "Dielectric properties and optical phonons in $LiNbO_3$," *Phys. Rev.*, vol. 158, no. 2, pp. 433–445, 1967.

[17] C. Garrett, "Nonlinear optics, anharmonic oscillators, and pyroelectricity," *IEEE J. Quantum Elect.*, vol. 4, no. 3, pp. 70–84, Mar. 1968.

[18] D. A. Kleinman, "Nonlinear dielectric polarization in optical media," *Phys. Rev.*, vol. 126, no. 6, pp. 1977–1979, 1962.

[19] G. D. Boyd, T. J. Bridges, M. A. Pollack, and E. H. Turner, "Microwave nonlinear susceptibilities due to electronic and ionic anharmonicities in acentric crystals," *Introduction Electro Optic Devices*, vol. 26, no. 7, pp. 387–390, 1974.

[20] I. P. Kaminow and W. D. Johnston, "Quantitative determination of sources of the electro-optic effect in $LiNbO_3$ and $LiTaO_3$," *Phys. Rev.*, vol. 160, no. 3, pp. 519–522, 1967.

[21] H. Wondratschek, *International Tables for Crystallography*. New York, NY, USA: Springer, 2004.

[22] B. Carnahan, H. A. Luther, and J. O. Wilkes, "Applied numerical methods," *Math. Comput.*, vol. 24, no. 111, pp. 750–768, 1990.

[23] V. A. Bokil, Y. Cheng, Y. Jiang, and F. Li, "Energy stable discontinuous Galerkin methods for Maxwell's equations in nonlinear optical media," *J. Comput. Phys.*, vol. 350, pp. 1–33, 2017.

[24] A. Kitamoto, I. Shoji, M. Shirane, R. Ito, and T. Kondo, "Absolute scale of second-order nonlinear-optical coefficients," *J. Opt. Soc. Amer. B*, vol. 14, no. 9, pp. 2268–2294, 1997.